SCIENCE CHINA
Technological Sciences

Special Topic: Structural Integrity
•Article•

December 2021 Vol.64 No.12: 2577–2585
https://doi.org/10.1007/s11431-020-1872-8

Compliance-based testing method for fatigue crack propagation rates of mixed-mode I-II cracks

QI Shuang[1,2,3*], XIANG WenXin[2], CAI LiXun[1*], LIU XiaoKun[1], SHAO ChunBing[2], NING FangMao[2], SHI JinHua[3] & YU WeiWei[3]

[1] *Applied Mechanics and Structure Safety Key Laboratory of Sichuan Province, School of Mechanics and Engineering, Southwest Jiaotong University, Chengdu 610031, China;*
[2] *Taishan Nuclear Power Joint Venture Co., Ltd., Jiangmen 529200, China;*
[3] *Power Plant Life Management Research Center, Suzhou Nuclear Power Research Institute, Suzhou 215004, China*

Received December 24, 2020; accepted June 4, 2021; published online August 4, 2021

Mixed-mode I-II crack-based fatigue crack propagation ($FCP_{I\text{-}II}$) usually occurs in engineering structures; however, no theoretical formula or effective compliance test methods have been established for $FCP_{I\text{-}II}$ to date. For mixed-mode I-II flawed components, based on the principle of mean-value energy equivalence, we propose a theoretical method to describe the relationship between material elastic parameters, geometrical dimensions, load (or displacement), and energy. Based on the maximum circumferential stress criterion, we propose a uniform compliance model for compact tensile shear (CTS) specimens with horizontal cracks deflecting and propagating (flat-folding propagation) under different loading angles, geometries, and materials. Along with an innovative design of the fixture of CTS specimens used for $FCP_{I\text{-}II}$ tests, we develop a new compliance-based testing method for $FCP_{I\text{-}II}$. For the $30Cr_2Ni_4MoV$ rotor steel, the FCP rates of mode I, mode II, and mixed-mode I-II cracks were obtained via FCP tests using compact tension, Arcan, and CTS specimens, respectively. The obtained da/dN versus ΔJ curves of the FCP rates are close. The loading angle α and dimensionless initial crack length a_0/W demonstrated negligible effects on the FCP rates. Hence, the FCP rates of mode I crack can be used to predict the residual life of structural crack propagation.

finite element analysis, mixed-mode I-II crack, fatigue crack propagation rate, energy equivalence principle, testing method

Citation: Qi S, Xiang W X, Cai L X, et al. Compliance-based testing method for fatigue crack propagation rates of mixed-mode I-II cracks. Sci China Tech Sci, 2021, 64: 2577–2585, https://doi.org/10.1007/s11431-020-1872-8

1 Introduction

For characterizing the fatigue failure of materials, the rate of fatigue crack propagation (FCP) is a critical index of mechanical properties and is an essential basis for structural integrity assessment of crucial projects such as nuclear reactor engineering, chemical engineering, aeronautics and astronautics, and high-speed railway. Research on the FCP behavior primarily focuses on mode I cracks, whereas cracks in actual engineering components, such as pressure vessels, pipes, and aircraft skins, are mixed-mode I-II cracks under the plane stress state.

In the past three decades, mixed-mode I-II crack-based fatigue crack propagation ($FCP_{I\text{-}II}$) has been studied using different specimen geometries and testing methodologies. Certain studies [1–4] have proposed >10 geometries of specimens for quasi-static, cyclic loading for mixed-mode I-II crack propagation tests. In 1985, Richard [1] proposed a mixed-mode I-II compact tensile shear (CTS) specimen (Figure 1). W is the width, α is the loading angle, a_0 is the

*Corresponding authors (email: daisy_qishuang@126.com; lix_cai@263.net)

initial crack length, S_8 is twice the horizontal loading hole spacing, and S_9 is the vertical distance of the loading hole from the crack surface. Three pins are used to connect the CTS specimen with the device to achieve I-II loading with different mixing degrees. As shown in Figure 1, the applied load P can be decomposed into P_1, P_2, P_3, P_4, P_5, and P_6 [5,6], which can be expressed as follows:

$$\begin{cases} P_1 = P_6 = P\left(\dfrac{1}{2}\cos\alpha + \dfrac{S_9}{S_8}\sin\alpha\right), \\ P_2 = P_5 = P\sin\alpha, \\ P_3 = P_4 = P\left(\dfrac{1}{2}\cos\alpha - \dfrac{S_9}{S_8}\sin\alpha\right). \end{cases} \tag{1}$$

Heirani and Farhangdoost [7,8] investigated the rate and path of fatigue crack growth subjected to mixed-mode I-II loading under tensile and compressive stresses. Kim and Kim [9] and Peixoto and Castro [10] performed many experiments on CTS specimens subjected to a multiangle loading. In these experiments, because there is a gap between the CTS specimen and the loading device, it is difficult to ensure that the specimen is centered in the thickness direction, which may cause the asymmetric propagation of the crack along the thickness.

Accurate measurement of the FCP length and direction is important in studying $\mathrm{FCP_{I\text{-}II}}$ behavior. In 1978, Arcan et al. [11] proposed a shear butterfly specimen (Arcan specimen) and the loading device assembly, as shown in Figure 2. P is the applied load, and a_0 and W are the initial crack length and width of the Arcan specimen, respectively.

The mixed-mode crack propagation is deflected from its original path, making it difficult to measure the real-time crack length. For the propagation direction of the mixed-mode I-II crack, Erdogan and Sih [12], Richard et al. [13,14], Guo and Li [15] proposed the maximum circumferential stress (MCS), Richard, and configurational force-driven (C-force) criteria, respectively.

(1) Erdogan and Sih's criterion

Erdogan and Sih [12] proposed the MCS criterion to determine the $\mathrm{FCP_{I\text{-}II}}$ angle β as follows:

$$\beta = -\arccos\left(\frac{3K_{\mathrm{II}}^2 + K_{\mathrm{I}}\sqrt{K_{\mathrm{I}}^2 + 8K_{\mathrm{II}}^2}}{K_{\mathrm{I}}^2 + 9K_{\mathrm{II}}^2}\right), \tag{2}$$

where K_{I} and K_{II} are the tensile opening and sliding stress intensity factors (SIFs) of the mixed-mode I-II cracks, respectively.

(2) Richard's criterion

Richard et al. [13,14] established an approximate relationship between β, K_{I}, and K_{II} through multiple experiments to determine the crack deflection angle β.

$$\beta = \pm\left[155.5^\circ \frac{|K_{\mathrm{II}}|}{|K_{\mathrm{I}}| + |K_{\mathrm{II}}|} - 83.4^\circ \left(\frac{|K_{\mathrm{II}}|}{|K_{\mathrm{I}}| + |K_{\mathrm{II}}|}\right)^2\right]. \tag{3}$$

When $K_{\mathrm{II}}>0$, $\beta<0$, and vice versa.

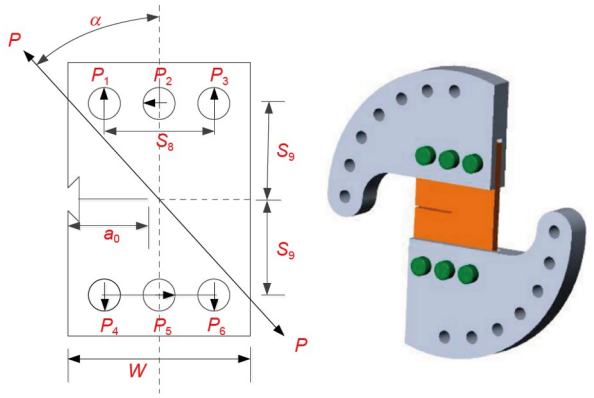

Figure 1 (Color online) Schematic of a CTS specimen and its loading device.

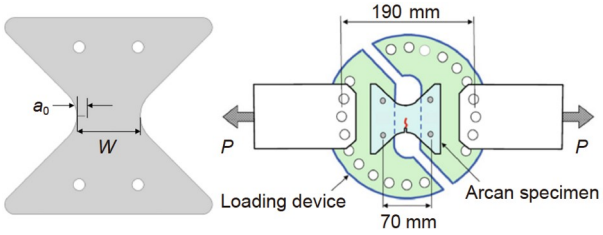

Figure 2 (Color online) Schematic of Arcan specimen and its loading device.

(3) C-force criterion

Guo and Li [15] proposed the C-force criterion describing the $\mathrm{FCP_{I\text{-}II}}$ law based on the physical interpretation of the C-forces at the crack tip defined by Eshelby [16]. The criterion assumes that the onset of crack growth occurs when the resultant C-force reaches a critical value, and this crack propagates in the direction of the resultant C-force. The initiation angle of the crack can be determined by

$$\begin{cases} \beta = \arctan\dfrac{C_1}{C_2}, \\ C_1 = \dfrac{K_{\mathrm{I}}^2 + K_{\mathrm{II}}^2}{E}, \\ C_2 = -\dfrac{2K_{\mathrm{I}}K_{\mathrm{II}}}{E}, \end{cases} \tag{4}$$

where C_1 and C_2 are the components of the C-force, which can be determined using K_{I}, K_{II}, and the elastic modulus E.

The mode I crack FCP ($\mathrm{FCP_I}$) test for crack length measurements is extensively used in the compliance test method. A CTS specimen with an extended oblique crack demonstrates significant theoretical difficulties from its unloading compliance. There is still no unified calculation formula for compliance. $\mathrm{FCP_{I\text{-}II}}$ compliance test methods based on CTS specimens are yet to be developed.

Here, for mixed-mode I-II cracks, based on the mean-value energy equivalence principle, we develop a theoretical method that describes the relationship between material elastic parameters, geometrical dimensions, load (or dis-

placement), and energy. We developed uniform models of compliance for CTS specimens with horizontal cracks deflecting and propagating (flat-folding propagation) under different loading angles, geometries, and materials. Then, we propose a new compliance-based testing method for $FCP_{I\text{-}II}$ (CTM-$FCP_{I\text{-}II}$).

2 Research conditions

2.1 Experiments on FCP

A turbine rotor material, $30Cr_2Ni_4MoV$ steel, was employed to perform FCP_I, FCP_{II}, $FCP_{I\text{-}II}$ rate tests using compact tension (CT), Arcan, and CTS specimens, respectively. The Young's modulus of elasticity and yield strength of the $30Cr_2Ni_4MoV$ steel are 202 and 794 MPa, respectively, as obtained by the uniaxial tensile tests of two round-bar tensile specimens. Figure 3 shows the dimensions of the CTS specimens used for the $FCP_{I\text{-}II}$ rate measurements. An innovatively designed extension fixture was employed in the $FCP_{I\text{-}II}$ test to assess the effect of different angles of fatigue loading on the CTS specimens. As shown in Figure 4, the improved extension fixture for $FCP_{I\text{-}II}$ was connected to a material test system (MTS) hydraulic chuck and the CTS specimen. The fixture was loaded in the directions of 0°, 15°, 30°, 45°, and 60°. The split clamp with the matching groove and specimen were connected with bolts; hence, the CTS specimen was successfully clamped.

A CTS specimen turns to a CT specimen when α is 0°. Figure 5 shows the CT specimen dimensions. Its width W and thickness B were 50 and 10 mm, respectively, and the initial crack length a_0 was 10 mm.

The CTS specimen turned to an Arcan specimen when α was 90°. Figure 6 shows the Arcan specimen dimensions. Its width W and thickness B were 30 and 1 mm, respectively. The initial crack length a_0 was 4 mm. As shown in Figure 7, the FCP_{II} extension fixture was connected to an MTS hydraulic chuck and the Arcan specimen. The static load of mode I was applied by bolt locking, and a load sensor of 5 kN was installed at the bottom of the bolt to monitor the static load during the test.

$FCP_{I\text{-}II}$, FCP_I, and FCP_{II} tests were conducted using an electromechanical test machine MTS810 with a load frame capacity of 25 kN under tension and an accuracy class of 0.5. A standard crack mouth opening displacement (CMOD) extensometer (MTS632.02F-20) with a gauge length of 5 mm and an accuracy class of 0.5 was used to measure the displacement of the CTS and CT specimens with a 4-mm-sized full range of displacement measurements.

For a 1- to 2-mm-long crack prefabricated for CTS, CT, and Arcan specimens, the loading angle α was 0°, loading ratio R was 0.1, and frequency f was 20 Hz. R and f for the FCP tests were the same as those of precracks. The FCP_I length for the CT specimens was measured in real-time using the compliance test method as per the ASTM E647-2013a standard. Tables 1 and 2 show the loading conditions for the CTS and Arcan specimens, respectively. In Table 2, speci-

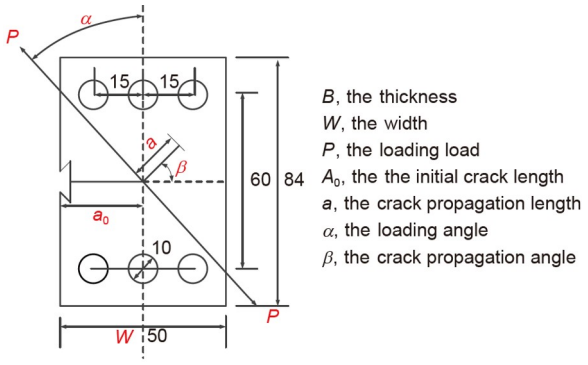

Figure 3 (Color online) Geometric dimensions of the CTS specimen (B= 5.26 mm).

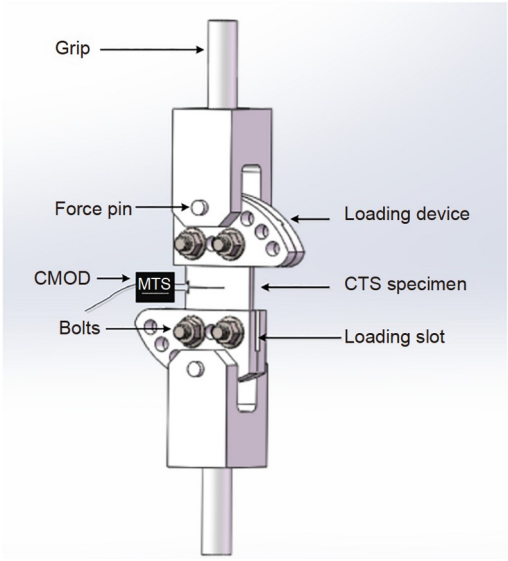

Figure 4 (Color online) Assembly drawing of the loading device for $FCP_{I\text{-}II}$ rate tests.

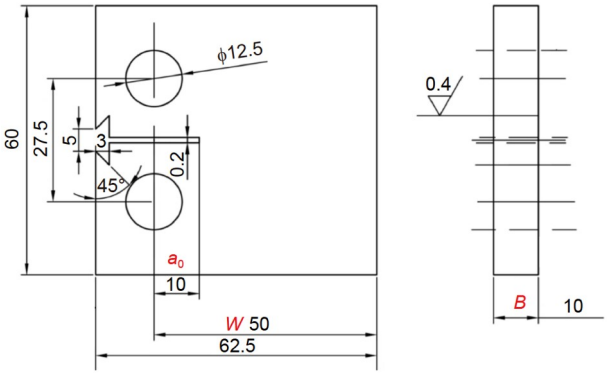

Figure 5 (Color online) Geometric dimensions of the CT specimen.

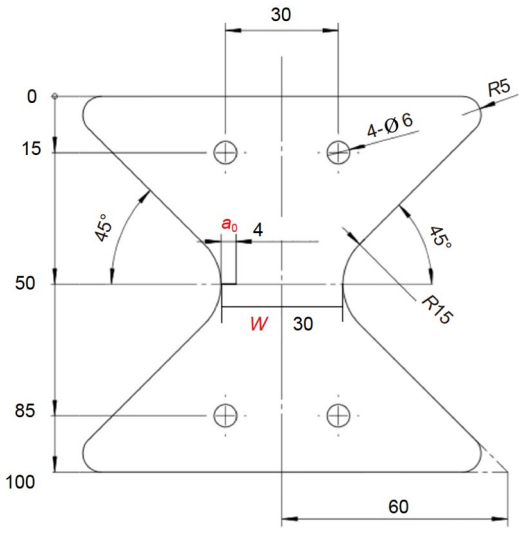

Figure 6 (Color online) Geometric dimensions of the Arcan specimen.

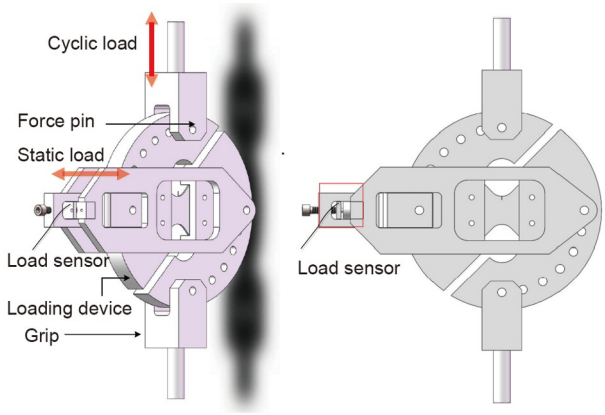

Figure 7 (Color online) Assembly drawing of the loading device for FCP_{II} rate tests.

mens 3# and 4# were under pure mode II loading, and specimens 1#, 2#, and 5# were subjected to both mode II cyclic loading and mode I static loading to study the influence of mode I static loading on the FCP_{II} rates. The FCP_{II} length of the Arcan specimens was measured by the vision: a scale was pasted on the Arcan specimen and cyclic images were taken at intervals.

2.2 Finite element analysis of CTS and Arcan specimens

Finite element analysis (FEA) was performed using the commercial code ANSYS 14.5. The FEA simulation is based on the assumption of continuous medium mechanics. In numerical simulations, coarse elements may generally affect FEA results, such as the load-displacement curve of a test specimen, but the meshed grids are fine. Before the FEA simulation, we compared the calculation results exposed to different mesh densities and selected the appropriate element

Table 1 Loading conditions for CTS specimens

Specimens	The initial crack a_0/W	Prefabricated crack a_0/W	Loading angle α (°)	Loading ratio R	Frequency f (Hz)	$P_{I\text{-}II\text{-}max}$ (N)
1#	0.3600	0.3813	15	0.1	20	8500
2#	0.4600	0.4730	15	0.1	20	6000
3#	0.5600	0.5902	15	0.1	20	4500
4#	0.3600	0.3725	30	0.1	20	8500
5#	0.4600	0.4810	30	0.1	20	6000
6#	0.5600	0.5834	30	0.1	20	4500
7#	0.5600	0.5777	30	0.1	20	4500
8#	0.3600	0.3762	45	0.1	20	8500
9#	0.4600	0.4728	45	0.1	20	6000
10#	0.5600	0.5898	45	0.1	20	4500
11#	0.3600	0.3682	60	0.1	20	8500
12#	0.4600	0.4753	60	0.1	20	6000
13#	0.5600	0.5719	60	0.1	20	4500

Table 2 Loading conditions for Arcan specimens

Specimens	The initial crack a_0/W	Prefabricated crack a_0/W	Loading ratio R	Frequency f (Hz)	$P_{II\text{-}max}$ (N)	$P_{I\text{-}static}$ (N)
1#	0.1333	0.1676	0.1	20	3200	1200
2#	0.1333	0.1661	0.1	20	3200	1200
3#	0.1333	0.2200	0.1	20	3250	0
4#	0.1333	0.1690	0.1	20	3250	0
5#	0.1333	0.1677	0.1	20	3500	1750

size.

Figures 8 and 9 show the CTS and Arcan specimen grid models, respectively. PLANE183 elements were used for the plane stress model with a thickness.

3 Compliance-based testing method for $FCP_{I\text{-}II}$

For monotonic-loaded experimental structural components with materials that meet isotropic and linear- or power-law constitutive relations, based on the principle of mean-value energy equivalence [17–19], we establish a theoretical method [20] to describe the relationship between material elastic parameters, geometrical dimensions, load (or displacement), and energy as follows:

$$\begin{cases} \dfrac{U_e}{U_e^*} = \begin{cases} \left(\dfrac{h}{h^*}\right)^2, \\ \left(\dfrac{P}{P_e^*}\right)^2, \end{cases} \\ P_e^* = kEA^*,\ U_e^* = \dfrac{kEV^*}{2},\ V^* = A^*h^*. \end{cases} \tag{5}$$

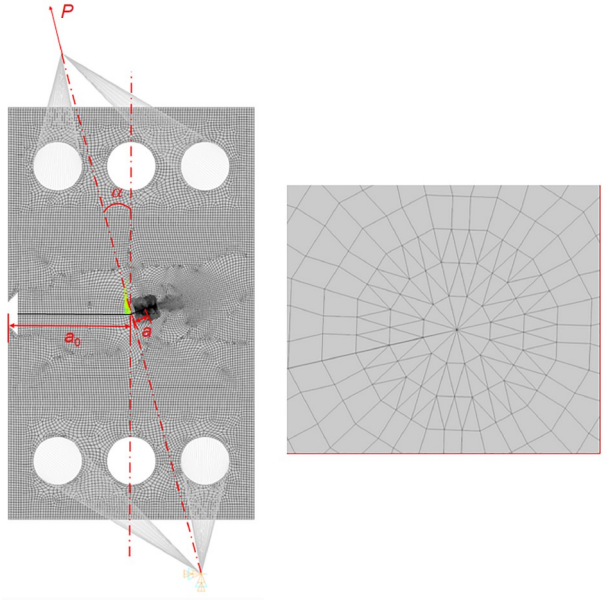

Figure 8 (Color online) Finite element model for a CTS specimen.

In eq. (5), P is the external load; h is the displacement; U_e is the elastic strain energy; h^* is the characteristic displacement, which can be taken as a single-size parameter of the constructor; P_e^* is the characteristic load; U_e^* is the characteristic energy; V^* is the characteristic volume; A^* is the characteristic area of the deformed region; and k is the parameter to be determined. U_e can then be obtained as follows from eq. (6):

$$U_e = \frac{P^2}{2Ek}\frac{h^*}{A^*}. \tag{6}$$

The principle of mean-value energy equivalence is the theoretical basis for $CTM\text{-}FCP_{I\text{-}II}$.

Under small-scale yielding conditions, as per the literature [21], the J-integral elastic component (J_e) is determined by

$$J_e = \frac{\partial U_e}{B\partial a_0}, \tag{7}$$

where B is the thickness of the specimen. Substituting U_e in eq. (6) into eq. (7):

$$J_e = \frac{P^2}{2BEk}\frac{\partial}{\partial a_0}\left(\frac{h^*}{A^*}\right). \tag{8}$$

J_e, which has the same value as energy release rate G_0, can be obtained through SIF (K) conversion when affected by a small range of plane stress yield, and its relationship is as follows:

$$G_0 = J_e = \frac{K^2}{E}, \tag{9}$$

where K can be expressed as follows:

$$K = \sqrt{\frac{P^2}{2Bk}\frac{\partial}{\partial a_0}\left(\frac{h^*}{A^*}\right)}. \tag{10}$$

Tanaka [22] considered that mode I loading and mixed-mode I-II cracks do not influence each other under small-scale yield conditions. For the structure with mixed-mode I-II cracks subjected to different loading angles, the tensile opening SIF (K_I) and sliding SIF (K_{II}) are expressed as follows:

$$K_i = \sqrt{\frac{P_i^2}{2Bk_i}\frac{\partial}{\partial a_0}\left(\frac{h^*}{A_i^*}\right)},\quad i = \mathrm{I, II}, \tag{11}$$

where $P_I(=P\cos\alpha)$ and $P_{II}(=P\sin\alpha)$ are the load experiencing modes I and II decomposition, respectively. A_I^* and A_{II}^* are the characteristic areas subjected to modes I and II loading,

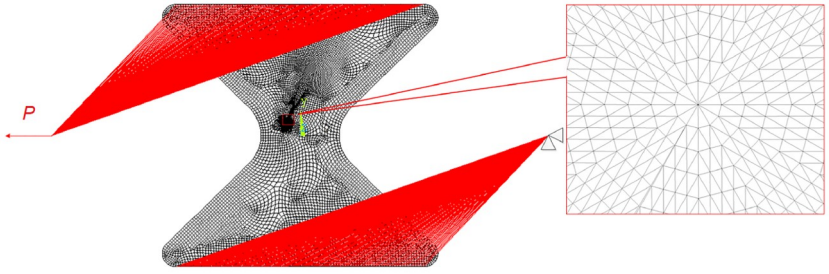

Figure 9 (Color online) Finite element model for an Arcan specimen.

respectively. They are both functions related to the length of the remaining ligament b_0, $b_0/W=1-a_0/W$, and h^* and A^* can be defined as follows:

$$\begin{cases} h^* = W, \\ A_i^* = WB \cdot f(b_0/W)_i, \quad i = \text{I, II}. \end{cases} \tag{12}$$

Then, the following expression can be obtained:

$$K_i = \sqrt{\frac{P_i^2}{2B^2 k_i} \frac{\partial \frac{1}{f(b_0/W)_i}}{\partial a_0}}, \quad i = \text{I, II}. \tag{13}$$

According to ref. [23], if the crack tip zone is in the small-scale yielding regime, J is equal to its elastic component J_e, expressed as follows:

$$J_e = \frac{K_I^2 + K_{II}^2}{E}. \tag{14}$$

Furthermore, J_e integral (J_{e0}) of the mixed-mode I-II specimens with a crack length of a_0 can be expressed as follows:

$$J_{e0} = \frac{P^2 \cos^2\alpha}{2BEk_I} \frac{\partial}{\partial a_0}\left(\frac{h^*}{A_I^*}\right) + \frac{P^2 \sin^2\alpha}{2BEk_{II}} \frac{\partial}{\partial a_0}\left(\frac{h^*}{A_{II}^*}\right). \tag{15}$$

The expressions for $f(b_0/W)_i$ can be obtained by FEA:

$$\begin{cases} f(b_0/W)_I = \exp[9.1493 + 21.5697(b_0/W) \\ \qquad\qquad - 14.8211(b_0/W)^{1.5}], \\ f(b_0/W)_{II} = 732102 + 3736633(b_0/W)^{1.5} \\ \qquad\qquad - 3295857(b_0/W)^2 - 69183/\ln(b_0/W). \end{cases} \tag{16}$$

For CTS specimens with initial horizontal cracks a_0, $k_I = k_{II} = 9.88614\times10^{-8}$, the ratio of the load-line displacement (LLD) δ_{LLD} to the load P is defined as the loading line compliance C_{LLD}:

$$C_{LLD} = \delta_{LLD}/P. \tag{17}$$

The compliance method is an important method to obtain the real-time FCP length. The Irwin-Kies [24] relationship is expressed as follows:

$$G_0 = \frac{P^2}{2}\frac{\partial C_{LLD}}{\partial A} = \frac{P^2}{2B}\frac{\partial C_{LLD}}{\partial a_0}, \tag{18}$$

where A is the area of the crack surface. According to eqs. (14), (15), (18),

$$\frac{\partial C_{LLD}}{\partial a_0} = \frac{\cos^2\alpha}{Ek_I} \frac{\partial}{\partial a_0}\left(\frac{h^*}{A_I^*}\right) + \frac{\sin^2\alpha}{Ek_{II}} \frac{\partial}{\partial a_0}\left(\frac{h^*}{A_{II}^*}\right). \tag{19}$$

C_{LLD} is described as follows:

$$\begin{cases} C_{LLD} = C_{I\text{-}LLD} + C_{II\text{-}LLD}, \\ \begin{cases} C_{I\text{-}LLD} = \dfrac{\cos^2\alpha}{Ek_I}\dfrac{h^*}{A_I^*}, \\ C_{II\text{-}LLD} = \dfrac{\sin^2\alpha}{Ek_{II}}\dfrac{h^*}{A_{II}^*}, \end{cases} \end{cases} \tag{20}$$

where $C_{I\text{-}LLD}$ and $C_{II\text{-}LLD}$ are the equivalent compliance perpendicular and parallel to the direction of the initial crack surface, respectively. δ_{CMOD}/P is the equivalent compliance for CTS specimens with the initial horizontal crack, denoted as C_0^*. According to FEA, C_0^* can be obtained from eq. (20) as follows:

$$\begin{cases} C_0^* = g(C_{I\text{-}LLD}, C_{II\text{-}LLD}, \alpha) \\ \quad = 1/(4.59855\times10^{-1} - 2.64035\times10^{-1}\alpha^2 \\ \quad +4.92985\times10^{-2}\alpha^3) \times [1 - \exp(-C_{I\text{-}LLD})] \\ \quad + 8.64978\times10^{-6}\cos\alpha \cdot \ln(C_{II\text{-}LLD}), \\ \begin{cases} \alpha \in [0, \pi/2), \\ a_0/W \in [0.26, 0.74]. \end{cases} \end{cases} \tag{21}$$

Eq. (21) is called the C_0^*-CTS (C_0^* of CTS specimens with an initial horizontal crack) model.

δ_{CMOD}/P is the equivalent compliance of the CTS specimens with horizontal cracks deflecting and propagating (flat-folding propagation) under different loading angles denoted as C^*. According to FEA, C^* can be expressed as follows:

$$\begin{cases} \dfrac{C^*}{C_0^*} = \\ \dfrac{o_1 + o_2\cdot(a_0/W) + o_3\cdot(a_0/W)^2 + o_4\cdot(a/W) + o_5\cdot(a/W)^2}{1 + o_6\cdot(a_0/W) + o_7\cdot(a_0/W)^2 + o_8\cdot(a/W) + o_9\cdot(a/W)^2}, \\ \begin{cases} o_1 = o_{11} + o_{12}\cos\alpha\ln(\cos\alpha) + o_{13}\cos^2\alpha + o_{14}/\ln(\cos\alpha), \\ o_2 = o_{21} + o_{22}\cos\alpha\ln(\cos\alpha) + o_{23}\exp(\cos\alpha) \\ \qquad + o_{24}\cos\alpha/\ln(\cos\alpha), \\ o_3 = o_{31} + o_{32}\cos\alpha\ln(\cos\alpha) + o_{33}\exp(\cos\alpha) + o_{34}/\ln(\cos\alpha) \\ o_4 = o_{41} + o_{42}\cos\alpha + o_{43}\cos^2\alpha/\ln(\cos\alpha) + o_{44}\exp(\cos\alpha), \\ o_5 = o_{51} + o_{52}\cos^{2.5}\alpha + o_{53}\ln(\cos\alpha)/\cos\alpha + o_{54}/\cos^{1.5}\alpha, \\ o_6 = o_{61} + o_{62}\cos^{1.5}\alpha + o_{63}\cos^2\alpha, \\ o_7 = o_{71} + o_{72}\cos^{1.5}\alpha + o_{73}\cos^2\alpha, \\ o_8 = o_{81}/\{1 + \exp[-(\cos\alpha - o_{82})/o_{83}]\}, \\ o_9 = o_{91} + o_{92}\cos^{0.5}\alpha\ln\cos\alpha + o_{93}/\cos^2\alpha, \end{cases} \\ \begin{cases} \alpha \in [0, \pi/2), \\ a_0/W \in [0.36, 0.64], \\ a/W \in [0, 0.2]. \end{cases} \end{cases} \tag{22}$$

Eq. (22) is called the C^*-CTS (C^* of CTS specimens with horizontal cracks deflecting and propagating) model. Table 3 lists the o parameters.

When $\alpha\in[0, \pi/2)$, α is separated by $\pi/36$; when $a_0/W\in[0.36, 0.64]$, a_0/W is separated by 0.04; and when $a/W\in[0, 0.2]$, a/W is separated by 0.01. FEA results of C^*/C_0^* were obtained and compared with the prediction results of the C^*-CTS model, which shows a relative deviation of 95% in <1% of the data, and the maximum error is <4%. Figure 10 shows the C^*/C_0^* curves obtained using the C^*-CTS model and FEA for the CTS specimens in logarithmic coordinates.

Table 3 Parameters of the C^*-CTS model

o_{ij}	j=1	j=2	j=3	j=4
i=1	−1.72693	−5.97117	2.90343	0.0000866395
i=2	32.6188	28.6184	−12.2939	−0.00200
i=3	−36.4512	−32.0195	13.3136	0.000762505
i=4	−256.519	−570.407	−258.392	304.958
i=5	344.133	−29.2817	−382.188	−310.138
i=6	5.15725	−12.061	6.85455	–
i=7	−5.53482	9.21464	−4.545	–
i=8	−10.9332	0.63634	−0.35551	–
i=9	2.78443	−12.0932	0.051549	–

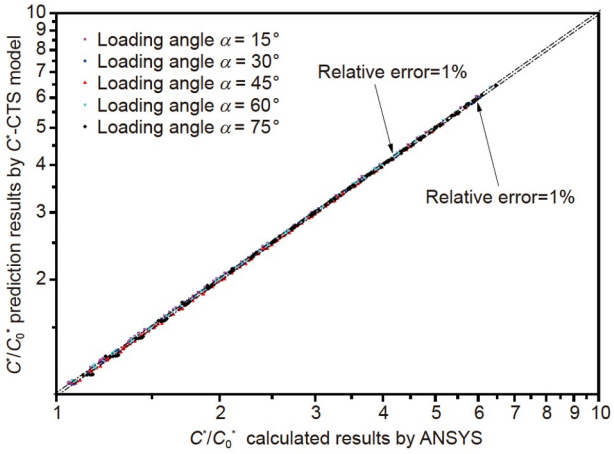

Figure 10 (Color online) C^*-CTS model prediction and FEA results for C^*/C_0^*.

The curves closely match; hence, the C^*-CTS model is effective and accurate under the given conditions. A novel CTM-FCP$_{\text{I-II}}$ is proposed for CTS specimens.

4 Results and discussion

4.1 Propagation angle of the mixed-mode I-II cracks

K_{I} and K_{II} analyses of CTS and Arcan specimens were performed using the grid model, as shown in Figures 8 and 9, respectively. Tables 4 and 5 show the prediction results of the FCP$_{\text{I-II}}$ and FCP$_{\text{II}}$ experimental propagation angles, respectively, as per the MCS, Richard, and C-force criteria.

For the Richard criterion, the FCP$_{\text{I-II}}$ prediction and test results for different loading angles show relative errors between 4% and 23%. For the C-force criterion, the predicted FCP$_{\text{I-II}}$ angle is consistent with that obtained from experiments at small loading angles; however, the prediction errors for the FCP$_{\text{I-II}}$ angle increased when the loading angle was >45°. For the MCS criterion, the prediction error for the FCP$_{\text{I-II}}$ angle is ~6%.

For the Richard criterion, the maximum relative error between the predicted FCP$_{\text{II}}$ angle and the test results is ~8.7%. The C-force criterion failed in the prediction of FCP$_{\text{II}}$. The relative errors for the MCS criterion for the FCP$_{\text{II}}$ angle are within 0.9%.

The FCP angle β for the CTS specimen was dependent on α and a_0/W. FCP$_{\text{I-II}}$ and FCP$_{\text{II}}$ propagated over a wide range in straight lines at near-constant angles. Compared with the Richard and C-force criteria, the MCS criterion showed higher prediction accuracy for the FCP$_{\text{I-II}}$ angle; hence, the MCS criterion was adopted for subsequent theories.

4.2 FCP rates

We conducted FCP$_{\text{I-II}}$ tests under certain loading ratios and angles for the CTS specimen with an initial precrack length a_0. During the test, the load (P) and CMOD (δ_{CMOD}) data and

Table 4 Experimental and predicted crack propagation angle β and the relative errors for CTS specimens

Specimens	Experimental		MCS criterion		Richard criterion		C-force criterion	
	α (°)	β (°)	Predicted results β (°)	Relative error (%)	Predicted results β (°)	Relative error (%)	Predicted results β (°)	Relative error (%)
1#	15	15.93	16.45	3.280	18.95	18.97	16.44	3.189
2#	15	14.36	14.97	4.248	17.62	22.70	15.23	6.059
3#	15	12.45	12.01	3.534	14.31	14.94	12.10	2.811
4#	30	30.55	30.90	1.138	33.20	8.679	30.53	0.08045
5#	30	28.09	28.63	1.922	30.98	10.29	28.50	1.463
6#	30	23.96	24.16	0.8347	26.62	11.10	24.24	1.169
7#	30	25.13	24.60	2.109	27.05	7.640	24.52	2.427
8#	45	43.16	42.74	0.2626	45.23	6.103	40.58	5.982
9#	45	38.97	40.82	4.747	43.20	10.85	39.24	0.6928
10#	45	33.52	35.35	5.459	37.62	12.23	34.84	3.938
11#	60	54.29	52.84	2.668	56.55	4.180	44.99	17.11
12#	60	50.01	51.23	2.440	54.68	9.338	44.82	10.38
13#	60	46.71	47.70	2.120	50.62	8.371	43.66	6.530

Table 5 Experimental and predicted crack propagation angle β and the relative errors for Arcan specimens

Specimens	Experimental		MCS criterion		Richard criterion		C-force criterion	
	α (°)	β (°)	Predicted results β (°)	Relative error (%)	Predicted results β (°)	Relative error (%)	Predicted results β (°)	Relative error (%)
1#	90	57.4	57.63	0.4044	62.27	8.745	43.45	24.3
2#	90	58.8	58.5	0.5058	63.3	7.654	42.67	27.4
3#	90	70.4	70.53	0.1829	72.01	2.415	0	100
4#	90	70.1	70.53	0.6079	72.01	2.774	0	100
5#	90	55.6	55.11	0.8744	59.25	6.168	44.73	19.54

the corresponding number of cycles were recorded using a computer. The C^*-CTS model was employed to calculate the crack deflection propagation length a of the CTS specimen in real-time. The J-integral range ΔJ was obtained by FEA. Figure 11 shows the relationship between the $FCP_{I\text{-}II}$ rate da/dN and ΔJ.

For the $30Cr_2Ni_4MoV$ rotor steel, the $FCP_{I\text{-}II}$ tests were performed for CTM-$FCP_{I\text{-}II}$ using CTS specimens at loading angles of 15°, 30°, 45°, and 60°. The FCP_I and FCP_{II} tests were performed using the CT and Arcan specimens, respectively. The obtained da/dN versus ΔJ curves are shown in Figures 12 and 13.

The results of FCP_{II} tests under five conditions are consistent. Combining with the analysis results in Table 2, the static load of mode I has effects on the direction of FCP_{II}.

Figure 14 shows that for the $30Cr_2Ni_4MoV$ rotor steel, da/dN versus ΔJ curves of FCP_I, FCP_{II}, and $FCP_{I\text{-}II}$ are consistent, nearly the same dispersion zone. The loading angle α and dimensionless initial crack length a_0/W have negligible effects on the FCP rates; hence, the FCP_I test results can be used to predict the residual life of structural crack propagations.

5 Conclusions

For mixed-mode I-II flawed components, we propose a theoretical method based on the principle of mean-value energy equivalence to describe the relationship between the material elastic parameters, geometrical dimensions, load (or displacement), and energy.

Based on the MCS criterion, we established the compliance models for CTS specimens with horizontal cracks deflecting and propagating (flat-folding propagation) under different loading angles, geometries, and materials. Combined with an innovative design of the fixture of the CTS

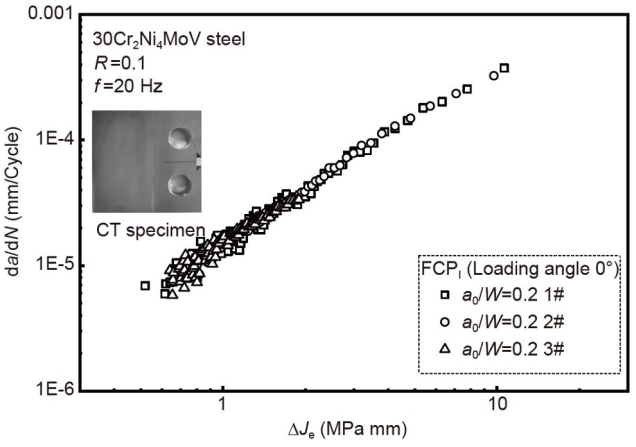

Figure 12 da/dN versus ΔJ curves obtained from FCP_I tests for the $30Cr_2Ni_4MoV$ steel.

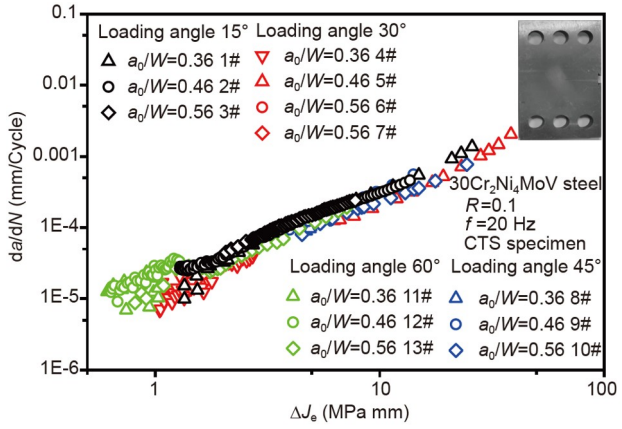

Figure 11 (Color online) da/dN versus ΔJ curves obtained from $FCP_{I\text{-}II}$ tests for the $30Cr_2Ni_4MoV$ steel.

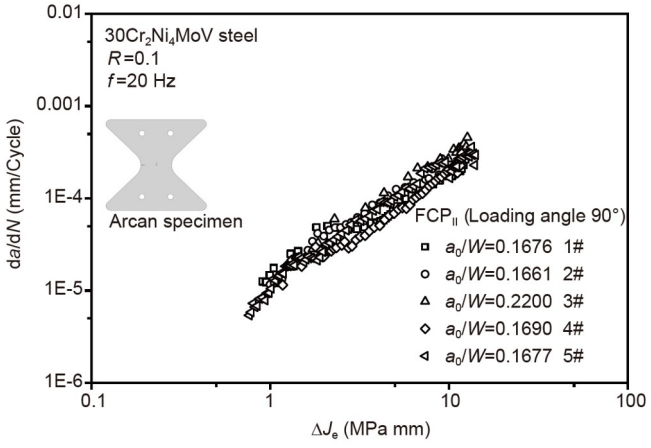

Figure 13 da/dN versus ΔJ curves obtained from FCP_{II} tests for the $30Cr_2Ni_4MoV$ steel.

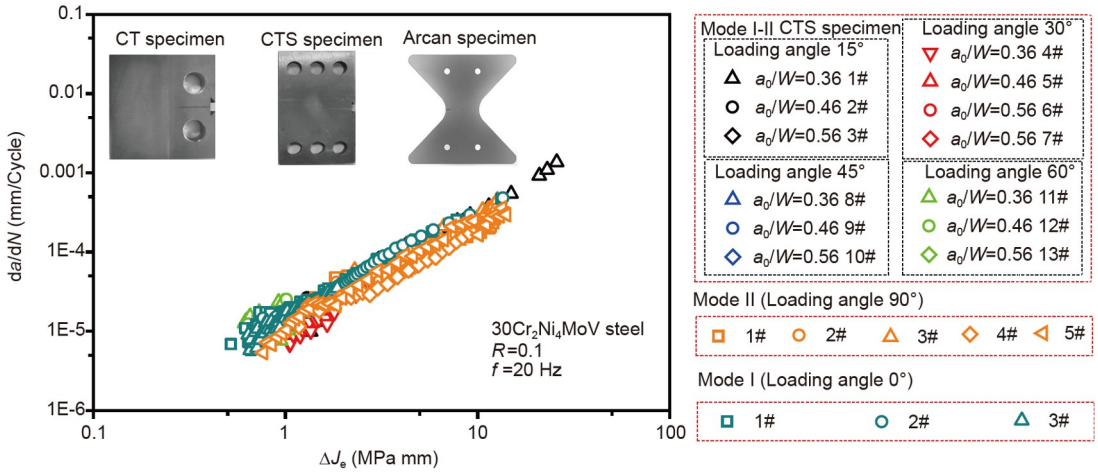

Figure 14 (Color online) da/dN versus ΔJ curves for the $30Cr_2Ni_4MoV$ steel.

specimen used for $FCP_{I\text{-}II}$ testing, we propose a new compliance-based testing method for $FCP_{I\text{-}II}$ (CTM-$FCP_{I\text{-}II}$). For CTS specimens whose initial horizontal crack length a_0 and subsequent inclined crack length a satisfy $a_0/W\in[0.36, 0.64]$ and $a/W\in[0, 0.2]$, respectively, when the loading angle α satisfies $\alpha\in[0, \pi/2)$, the predicted results of the compliance are in good agreement with the FEA results with relative errors of <1%.

A series of FCP tests for the $30Cr_2Ni_4MoV$ rotor steel was conducted using the CTM-$FCP_{I\text{-}II}$ method. The results of the FCP rate exposed to different loading angles and initial crack lengths were obtained. The da/dN versus ΔJ curves of FCP_I, FCP_{II}, and $FCP_{I\text{-}II}$ are consistent with nearly the same dispersion zone. Hence, the FCP_I test results can be used to predict the residual life of structural crack propagation.

This work was supported by the National Key Research and Development Program of China (Grant No. 2017YFB0702200), the National Natural Science Foundation of China (Grant No. 11872320), and the Policy Guidance Program of Jiangsu Province (Grant No. BZ2020057).

1 Richard H A. Specimens for investigating biaxial fracture and fatigue processes. In: Biaxial and Multiaxial Fatigue (EGF 3). Hoboken: John Wiley & Sons, Inc., 1989. 217–228
2 Mahanty D K, Maiti S K. Experimental and finite element studies on mode I and mixed mode (I and II) stable crack growth—I. Experimental. Eng Fract Mech, 1990, 37: 1237–1250
3 Buzzard R J, Gross B, Srawley J E. Mode II fatigue crack growth specimen development. In: Proceedings of National Symposium on Fracture Mechanics. Albany, 1983. 329–346
4 Otsuka A, Tohgo K, Matsuyama H. Fatigue crack initiation and growth under mixed mode loading in aluminum alloys 2017-T3 and 7075-T6. Eng Fract Mech, 1987, 28: 721–732
5 Richard H A, Benitz K. A loading device for the creation of mixed mode in fracture mechanics. Int J Fract, 1983, 22: R55–R58
6 Richard H A. Fracture Mechanical Predictions for Cracks with Superimposed Normal and Shear Loading. Düsseldorf: VDI-Verlag, 1985
7 Heirani H, Farhangdoost K. Mixed mode I/II fatigue crack growth under tensile or compressive far-field loading. Mater Res Express, 2017, 4: 116505
8 Heirani H, Farhangdoost K. Effect of compressive mode I on the mixed mode I/II fatigue crack growth rate of 42CrMo4. J Materi Eng Perform, 2018, 27: 138–146
9 Kim J K, Kim C S. Fatigue crack growth behavior of rail steel under mode I and mixed mode loadings. Mater Sci Eng-A, 2002, 338: 191–201
10 Peixoto D F C, de Castro P M S T. Mixed mode fatigue crack propagation in a railway wheel steel. Procedia Struct Integrity, 2016, 1: 150–157
11 Arcan M, Hashin Z, Voloshin A. A method to produce uniform plane-stress states with applications to fiber-reinforced materials. Exp Mech, 1978, 18: 141–146
12 Erdogan F, Sih G C. On the crack extension in plates under plane loading and transverse shear. J Basic Eng, 1963, 85: 519–525
13 Richard H A, Fulland M, Sander M. Theoretical crack path prediction. Fat Frac Eng Mat Struct, 2005, 28: 3–12
14 Richard H A, Schöllmann M, Fulland M, et al. Experimental and numerical simulation of mixed mode crack growth. In: Proceedings of the 6th International Conference on Biaxial/multiaxial Fatigue & Fracture. Lisbon, 2001. 623–30
15 Guo Y, Li Q. Material configurational forces applied to mixed mode crack propagation. Theor Appl Fract Mech, 2017, 89: 147–157
16 Eshelby J D. The elastic energy-momentum tensor. J Elasticity, 1975, 5: 321–335
17 Chen H, Cai L. Theoretical model for predicting uniaxial stress-strain relation by dual conical indentation based on equivalent energy principle. Acta Mater, 2016, 121: 181–189
18 Chen H, Cai L. Unified elastoplastic model based on a strain energy equivalence principle. Appl Math Model, 2017, 52: 664–671
19 Chen H, Cai L. An elastoplastic energy model for predicting the deformation behaviors of various structural components. Appl Math Model, 2019, 68: 405–421
20 Qi S, Cai L X, Bao C, et al. Analytical theory for fatigue crack propagation rates of mixed-mode I-II cracks and its application. Int J Fatigue, 2019, 119: 150–159
21 Rice J R. A path independent integral and the approximate analysis of strain concentration by notches and cracks. J Appl Mech, 1968, 35: 379–386
22 Tanaka K. Fatigue crack propagation from a crack inclined to the cyclic tensile axis. Eng Fract Mech, 1974, 6: 493–507
23 Shih C F. Elastic-plastic analysis of combined mode crack problems. Dissertation for Doctoral Degree. Cambridge: Harvard University. 1973. 1–3
24 Irwin G R. Analysis of stresses and strains near the end of a crack traversing a plate. J Appl Mech, 1957, 24: 361–364